APPLIED PHYSICS

Hamiltonian learning for 300 trapped ion qubits with long-range couplings

Shi-An Guo[1]†, Yu-Kai Wu[1,2,3]†, Jing Ye[1], Lin Zhang[1], Ye Wang[4], Wen-Qian Lian[4], Rui Yao[4], Yu-Lin Xu[1], Chi Zhang[4], Yu-Zi Xu[1], Bin-Xiang Qi[1], Pan-Yu Hou[1,2], Li He[1,2], Zi-Chao Zhou[1,2], Lu-Ming Duan[1,2,5]*

Quantum simulators with hundreds of qubits and engineerable Hamiltonians have the potential to explore quantum many-body models that are intractable for classical computers. However, learning the simulated Hamiltonian, a prerequisite for any quantitative applications of a quantum simulator, remains an outstanding challenge due to the fast increasing time cost with the qubit number and the lack of high-fidelity universal gate operations in the noisy intermediate-scale quantum era. Here, we demonstrate the Hamiltonian learning of a two-dimensional ion trap quantum simulator with 300 qubits. We use global manipulations and single-qubit–resolved state detection to efficiently learn the all-to-all–coupled Ising model Hamiltonian, with the required quantum resources scaling at most linearly with the qubit number. We further demonstrate a physically guided learning scheme with the quantum sample complexity independent of system sizes by carefully fitting the anharmonic trap potential. Our work paves the way for wide applications of large-scale ion trap quantum simulators.

INTRODUCTION

Quantum computers and quantum simulators have reached the stage of coherently manipulating hundreds of qubits (*1*–*4*), and quantum advantage over classical computers has been claimed in random sampling tasks (*5*–*9*). To achieve the next milestone of quantum advantage with practical utility, quantum simulation of many-body dynamics is one of the most promising candidates (*10*–*13*). However, verifying the quantum simulation results for such classically intractable problems is a notoriously challenging task. To completely characterize the simulated dynamics and to check whether it follows the desired Hamiltonian evolution, quantum process tomography requires a time cost that grows exponentially with the system size N (*14*). To reduce this complexity, various Hamiltonian learning algorithms have been developed (*15*–*32*), using different types of a priori knowledge about the system like locality (*15*, *17*, *18*, *21*–*25*, *27*, *30*–*32*) and sparsity (*20*, *26*, *29*) or using the help of certain steady states or thermal states (*22*–*25*, *31*) or other trusted quantum devices (*16*, *19*, *28*) as quantum resources. Nevertheless, a poly(N) time complexity is generally inevitable, which becomes a considerable cost for the large-scale quantum simulators. Besides, many of the learning algorithms require individually addressed quantum gates (*15*, *17*, *18*, *22*–*25*, *28*–*32*), which may not be available on the noisy intermediate-scale quantum (NISQ) devices.

On the other hand, quantum simulators based on arrays of atoms (*33*–*35*) or ions (*4*, *12*) can naturally support single-shot readout of all the N qubits, giving N bits of information per trial. This can largely reduce the required quantum simulation resource costs by up to a factor of N. Following this idea, the coherent imaging spectroscopy technique has been developed, where all the $O(N^2)$ coefficients in a fully connected Ising model can be determined from $O(N)$ frequency scans with global quantum manipulation and individual state detection (*36*). However, this scheme is subject to a lower signal-to-noise ratio as the state preparation error accumulates with increasing N. In addition, the time for each frequency scan may need to scale polynomially with N to resolve the decreasing energy gaps. Because of these restrictions, this scheme has only been applied to measure an eight-spin Hamiltonian (*36*) and to partially verify the theoretical calculations for 61 qubits (*37*).

Here, we report the Hamiltonian learning of an ion trap quantum simulator with 300 qubits. We use global laser and microwave operations to perform a Ramsey-type experiment with various evolution times under the desired Ising Hamiltonian. We extract single-spin and two-spin observables from the single-shot measurements to fit all the $O(N^2)$ Ising coupling coefficients (44,850 in total), and we test the learning results on independent data to show that there is no substantial overfitting. We further compare this general model to a physically guided one with $O(N)$ parameters. By independently calibrating the collective phonon modes of the ions and the laser intensity, the latter learning algorithm can achieve a similar test error as the former, with an improved scaling for the required sample size. We further compute the dynamics of higher-order spin correlations from the learned Hamiltonian and validate the learning results from their consistency with the experimental data. Our method can be applied to even larger ion crystals and paves the way for the applications of the ion trap quantum simulators on various NISQ algorithms (*11*, *13*).

RESULTS

Experimental scheme

Our experimental setup is sketched in Fig. 1A with a two-dimensional (2D) crystal of 300 $^{171}Yb^+$ ions in a cryogenic monolithic ion trap (*4*). The qubits are encoded in the hyperfine ground states $|0\rangle \equiv |S_{1/2}, F=0, m_F=0\rangle$ and $|1\rangle \equiv |S_{1/2}, F=1, m_F=0\rangle$. By applying counter-propagating 411-nm global laser beams on the ions perpendicular to the 2D crystal, we can generate a long-range Ising Hamiltonian $H_0 = \sum_{i<j} J_{ij}\sigma_z^i\sigma_z^j$ intermediated by the transverse (drumhead) phonon modes (*4*, *38*). When supplemented by a global microwave resonant to the qubit frequency, a transverse-field

[1]Center for Quantum Information, Institute for Interdisciplinary Information Sciences, Tsinghua University, Beijing 100084, PR China. [2]Hefei National Laboratory, Hefei 230088, PR China. [3]Shanghai Qi Zhi Institute, AI Tower, Xuhui District, Shanghai 200232, China. [4]HYQ Co. Ltd., Beijing 100176, PR China. [5]New Cornerstone Science Laboratory, Beijing 100084, PR China.
*Corresponding author. Email: lmduan@tsinghua.edu.cn
†These authors contributed equally to this work.

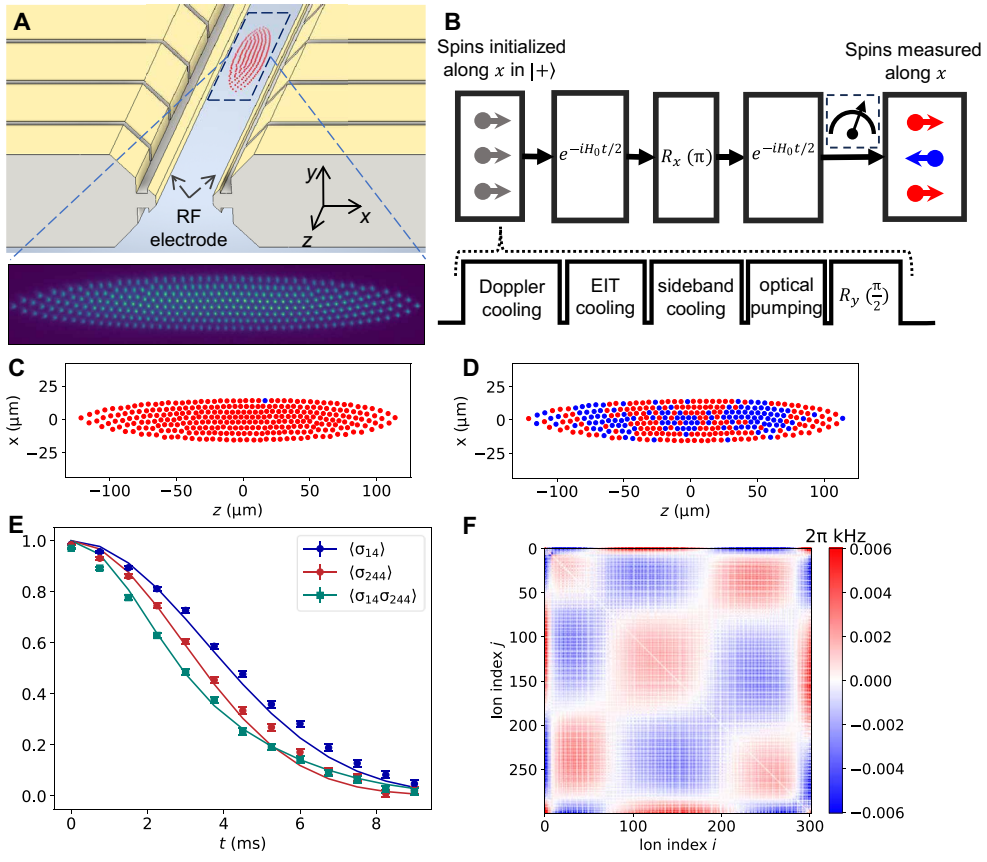

Fig. 1. Experimental scheme. (**A**) A cryogenic monolithic ion trap is used to obtain a two-dimensional (2D) crystal of $N = 300$ $^{171}Yb^+$ ions. (**B**) A Ramsey-type experiment is performed to learn the long-range Ising Hamiltonian using global control and individual readout of the qubits. We initialize all the ions in $|0\rangle$ by laser cooling and optical pumping and rotate them into $|+\rangle$ by a microwave $\pi/2$ pulse. The system is then evolved under the Ising Hamiltonian H_0 for various times t with a spin echo in the middle to cancel the longitudinal fields. Last, we measure all the ions in the σ_x basis via another microwave $\pi/2$ pulse followed by the state-dependent fluorescence detection. (**C**) Typical single-shot measurement result at $t = 0$ ms. (**D**) Typical single-shot measurement result at $t = 9$ ms. (**E**) All the single-spin (magnetization) and two-spin (correlation) observables are used to fit the Ising coupling coefficients. Typical fitting results (solid curves) are compared with the measured data (dots for magnetization and squares for correlation with one SD error bar) for an arbitrarily chosen ion pair. (**F**) The fitted Ising coupling coefficients J_{ij} when the laser couples dominantly to the fifth highest phonon mode.

Ising model $H = H_0 + B\sum_i \sigma_x^i$ can be obtained (*4*) with wide applications in quantum many-body physics (*12*) and NISQ algorithms (*11*, *13*). Because the transverse field B can be accurately controlled and separately calibrated in experiments, here, we focus on the calibration of the Ising coupling coefficients J_{ij}'s, which represents the challenging part of the Hamiltonian H to be learned. Theoretically, with the 2D crystal locating on an equiphase surface of the laser (see Materials and Methods) and under the virtual excitation condition of the phonon modes (*4*, *12*), the coupling coefficients can be given as

$$J_{ij} = \sum_k \frac{1}{8(\mu - \omega_k)} \eta_k^2 b_{ik} b_{jk} \Omega_i \Omega_j \qquad (1)$$

where μ is the laser detuning, ω_k is the frequency of the kth mode, η_k is the Lamb-Dicke parameter, Ω_i is the laser-induced ac Stark shift on the ith ion, and b_{ik} is the normalized mode vector.

The experimental sequence for Hamiltonian learning is shown in Fig. 1B where we perform a Ramsey-type experiment to extract information about H_0 by tuning the transverse B field to zero. We initialize the spins in $|+\rangle$ by a global microwave $\pi/2$ pulse, evolve them under H_0 for time t, and, lastly, measure all the spins in the σ_x basis by applying another microwave $\pi/2$ pulse followed by the site-resolved fluorescence detection. To remove the influence of possible longitudinal fields $H' = \sum_i h_i \sigma_z^i$ (which can be calibrated separately if needed), we apply a microwave π pulse in the middle of the Hamiltonian evolution that commutes with the desired H_0. A typical single-shot measurement result at $t = 0$, using the electron shelving technique (*39*–*41*), is shown in Fig. 1C with a few random spins being flipped due to the about 0.7% state-preparation-and-measurement (SPAM) errors. Similarly, in Fig. 1D, we show a typical single-shot measurement result at $t = 9$ ms when the Ising interaction is dominated by the pattern of the fifth highest phonon mode. By further averaging over M experimental trials, we can estimate any k-body spin correlation functions. Here, we focus on the single-spin ("magnetization") and two-spin ("correlation") observables and use them to fit all the J_{ij}'s, as shown in Fig. 1 (E and F). Later, we will use higher-order correlations to verify the Hamiltonian learning results.

Suppose we take data from T different evolution times. The NT magnetizations and $N(N-1)T/2$ correlations contain sufficient information to learn the $N(N-1)/2$ Ising coupling coefficients. Actually, in principle, even the early-time dynamics

$\langle \sigma_i(t)\sigma_j(t)\rangle - \langle \sigma_i(t)\rangle \langle \sigma_j(t)\rangle \approx 4|J_{ij}|^2 t^2$ is sufficient to determine the magnitude of all the J_{ij}'s. Here, we use longer evolution time and the analytical formulae for the magnetizations and correlations (see Materials and Methods) to fit the Ising coefficients so that the results will be more robust to the experimental noises. Because of the symmetry of the Hamiltonian and the initial state, the measured dynamics will be invariant if we change $J_{ij} \to -J_{ij}$ $(\forall j \neq i)$ for any given spin i. In other words, there exist an exponential number of equivalent solutions under our experimental sequence, which, in principle, can be distinguished by preparing different initial states. However, note that these equivalent patterns are discrete and well separated from each other given that each spin is strongly coupled to at least one of other spins. Therefore, we can simply use the theoretical predictions like Eq. 1 as the starting point of the fitting to break their symmetry.

We demonstrate this Hamiltonian learning algorithm for different Ising coupling coefficients in Fig. 2, with the laser dominantly coupled to the highest (center of mass) or the fifth phonon mode, or using two frequency components to couple to both of them (*4*). As shown in Fig. 2A, the residual sum of squares (RSS) of the least square fitting follows a $1/M$ scaling (solid curves) versus the sample size M at each time point due to the statistical fluctuation. There also exists a nonzero RSS in the limit $M \to \infty$ due to the deviations from the ideal fitting model caused by the SPAM error, the nonzero phonon excitations, and the spin dephasing due to high-frequency noise. (The dominant dephasing source of a shot-to-shot laser intensity fluctuation has been included in the theoretical model as described in Materials and Methods.) If we view the least square fitting as an optimization problem, then the RSS is already close to the $M \to \infty$ case (horizontal dashed lines) with about $M = 5000$ samples. However, this does not exclude the possible overfitting in the obtained Ising coefficients. For this purpose, we further plot the learning curve during the training process in Fig. 2B. We randomly split the data at each time point into two equal halves as the training and the test sets. We minimize the RSS of the training set by iterative algorithms and also compute the corresponding RSS on the test set at each step. As we can see, for all the three Hamiltonians to be learned, the RSS for the training and the test sets shows the same tendency and similar final values. This suggests that our sample size is large enough to avoid overfitting in the learning results.

Nevertheless, it is still desirable to have more samples to improve the precision. To quantify the precision of the learned Ising Hamiltonian, here, we define a relative energy difference $\epsilon\left[J^{(1)}, J^{(2)}\right] \equiv \langle |E\left[J^{(1)}\right] - E\left[J^{(2)}\right]| \rangle / \sqrt{\delta E\left[J^{(1)}\right] \cdot \delta E\left[J^{(2)}\right]}$, where the numerator is the energy difference between two sets of Ising coefficients $J_{ij}^{(1)}$'s and $J_{ij}^{(2)}$'s averaged over all the spin configurations, and the denominator consists of the SD of the energy for the two sets, again over all the spin configurations (see Materials and Methods for details). Roughly speaking, this quantity characterizes the phase difference accumulated during the typical timescale of the two Hamiltonians and has a scaling of $\sqrt{N}$ with the system size. Now, we can take two disjoint sets of data, each with M samples, to learn the Ising coupling coefficients $J^{(1)}$ and $J^{(2)}$, and compute their relative energy difference. We further average over random choices of the datasets to quantify the precision and fit a scaling $\epsilon \propto 1/\sqrt{M}$ as shown in Fig. 2C. From the fitting results, we can estimate that about 10^4 samples at each time point will be needed to reach a precision of 1 % for the $N = 300$ qubits. Note that the above definition of the precision is for general quantum dynamics and average spin configurations. In many cases, we will be interested in the ground states, then the undesired scaling of $\sqrt{N}$ can be removed, and the precision can be largely improved (see Materials and Methods). However, for general Ising Hamiltonian, the ground-state energy may be difficult to evaluate; therefore, here, we still use the above definition of the precision while recognizing that the actual precision may be better for certain tasks.

The above scaling of $\epsilon \propto \sqrt{N/M}$ suggests that, to reach the desired precision for large-scale quantum simulators, the required sample size M may scale linearly with the qubit number N. This can also be understood as follows: Although we use $O(N^2)$ observables (including magnetizations and correlations) to learn the $O(N^2)$

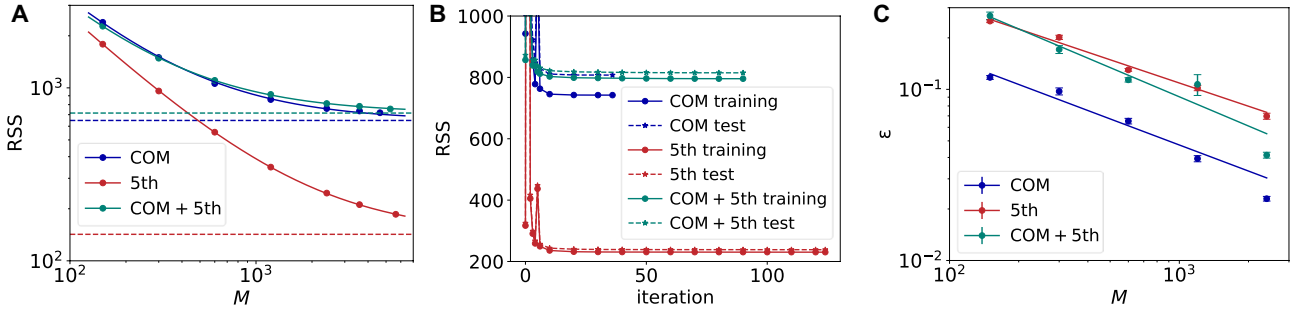

Fig. 2. Hamiltonian learning with $O(N^2)$ parameters. (**A**) Residual sum of squares (RSS) for $N = 300$ions and $T = 13$ time steps versus the sample size M at each step. Whether the Ising Hamiltonian comes from coupling to the first (blue) or the fifth (red) highest phonon mode or both (green), the experimental results can be well fitted by $y = ax^{-1} + b$ (solid curves) where $b > 0$ (horizontal dashed lines) corresponds to the deviation from the theoretical model due to experimental imperfections. After discarding the data when the configuration of the ion crystal is changed during the experimental sequence (see Materials and Methods), we get in total $M = 4638$, 5640, and 5272 samples for the three Hamiltonians, respectively. (**B**) Typical learning curves when we randomly divide the samples at each time point into two equal halves as the training and the test sets. We fit the Ising coupling coefficients J_{ij}'s using the training set by iteratively minimizing their RSS (training-RSS). For each step of iteration, we record the J_{ij}'s and compute the RSS on the test set (test-RSS). (**C**) Precision ϵ of the learning results versus the sample size M. We take two disjoint sets of data, each with M samples, to learn the Ising coupling coefficients separately. Then, we compute their relative energy difference for 1000 randomly sampled spin configurations. Last, we further average over five random choices of the disjoint datasets and use the SD as error bars. A scaling of $\epsilon \propto M^{-\alpha}$ is fitted with $\alpha \in [0.45, 0.57]$, close to the theoretical scaling of $M^{-0.5}$.

parameters of the Hamiltonian, note that they are computed from M single-shot measurement results that contain at most NM bits of information. In this sense, $M \sim O(N)$ samples will be necessary to estimate all the $O(N^2)$ parameters. To overcome this general scaling, additional knowledge about the physical system must be exploited to parameterize the Hamiltonian more economically. According to Eq. 1, one possibility is to calibrate the phonon modes and the laser intensities on all the ions. As shown in Fig. 3 (A and B) with more details in Materials and Methods, we can fit the anharmonic trap potential up to the fourth order from the measured equilibrium positions of the ions and a few phonon modes that can be resolved and further compute all the phonon mode structures theoretically. In addition, in Fig. 3C, we calibrate the laser intensity on individual ions by driving their carrier Rabi oscillations between the $S_{1/2}$ and $D_{5/2}$ levels. However, if we directly compute the Ising coupling coefficients using Eq. 1 (or add up two sets of such computed coefficients when applying two frequency components), then the performance of the learned Hamiltonian is typically not satisfactory, with much higher RSS on the test set as shown by the $O(1)$-scheme in Fig. 3D.

To understand the deviation from the above $O(N^2)$-scheme, we fix the calibrated phonon modes and turn the laser-induced ac Stark shift Ω_i into N fitting parameters. From Fig. 3D, we can see that, with these $O(N)$ fitting parameters, the RSS on the test data already becomes close to the $O(N^2)$-scheme. We plot the ratio between the fitted Ω_i and the measured ones in Fig. 3E when the laser couples dominantly to the fifth phonon mode. The discrepancy is most severe near the nodes of the fifth mode as shown in Fig. 3F where $b_{ik} \approx 0$ and near the edge of the 2D crystal with large micromotion of the ions. This suggests that the deviation between the $O(1)$-scheme and the $O(N^2)$-scheme is still restricted by the inaccurate calibration of the phonon modes and may be improved in the future by including the micromotion into the theoretical model. It also means that the $O(N)$ fitting parameters do not have the physical meaning of the laser intensity but are to compensate the miscalibrated phonon modes. Therefore, for the Hamiltonian when the laser has two frequency components to couple to two phonon modes, we should introduce N independent fitting parameters for each mode.

Predicting higher-order correlations

Apart from explaining all the magnetizations and the correlations, the learned Hamiltonian should also be able to predict the dynamics of higher-order spin correlations. As shown in Materials and Methods, for our experimental sequence, each k-body correlation can be computed analytically with a time cost of $O(2^k)$, and there are $O(N^k)$ such terms for small k. Therefore, instead of testing all of them or even including them in the Hamiltonian learning process, here, we choose to validate the learning results using a few randomly selected sets of ions. As shown in Fig. 4, we use the learning results of the $O(N^2)$-scheme, which come from all the single-spin and two-spin observables, to predict the dynamics of k-body correlations with

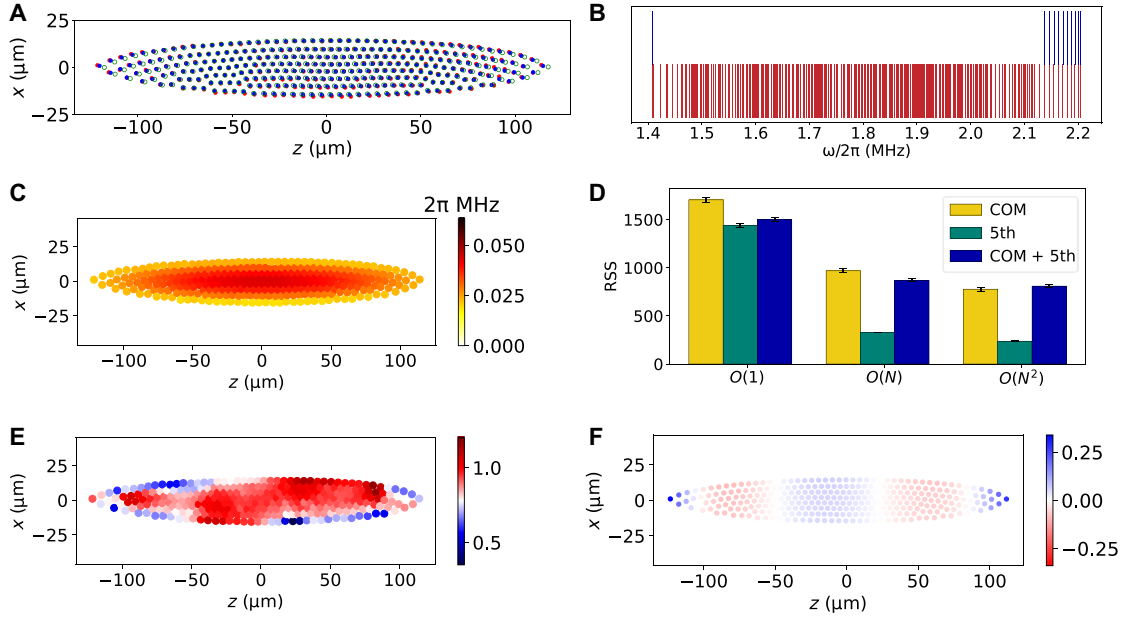

Fig. 3. Hamiltonian learning with $O(N)$ physically guided parameters. (**A** and **B**) Calibration of anharmonic trap potential. (A) Blue dots are the measured ion positions from the complementary metal-oxide semiconductor (CMOS) camera. Green hollow circles are the best fit assuming a quadratic potential in the *xz* plane. Red dots further include cubic and quartic terms in the potential. (B) Blue vertical lines are the measured transverse phonon mode frequencies. The phonon spectrum becomes too dense to resolve at the low-frequency side, so we measure the 10 highest phonon mode frequencies and one lowest frequency. Red vertical lines are the best-fitted theoretical mode frequencies with cubic and quartic potentials. (**C**) ac Stark shift Ω_i of individual ions from experimentally calibrated Rabi rates. They can further be fitted by a Gaussian profile with a full width at half maximum of 241 μm along the *z* direction and 29 μm along the *x* direction. (**D**) Comparison of test-RSS for Hamiltonian learning with $O(1)$, $O(N)$, and $O(N^2)$ parameters. Here, $O(N^2)$-scheme is the method in Fig. 2, $O(1)$-scheme is to compute the J_{ij} coefficients from the above calibrated phonon modes and laser intensities, while $O(N)$-scheme is to use the calibrated phonon modes but fit Ω_i's as free parameters. The yellow, green, and blue bars correspond to the Ising Hamiltonian when coupling to the first, fifth, or both phonon modes, respectively. Error bars represent one SD when randomly splitting the data into training and test sets for 10 times. (**E**) Ratio of the fitted Ω_i's for the $O(N)$-scheme to the calibrated values in the $O(1)$-scheme, when the laser couples mainly to the fifth phonon mode. (**F**) Mode structure b_{ik} of the fifth highest phonon mode.

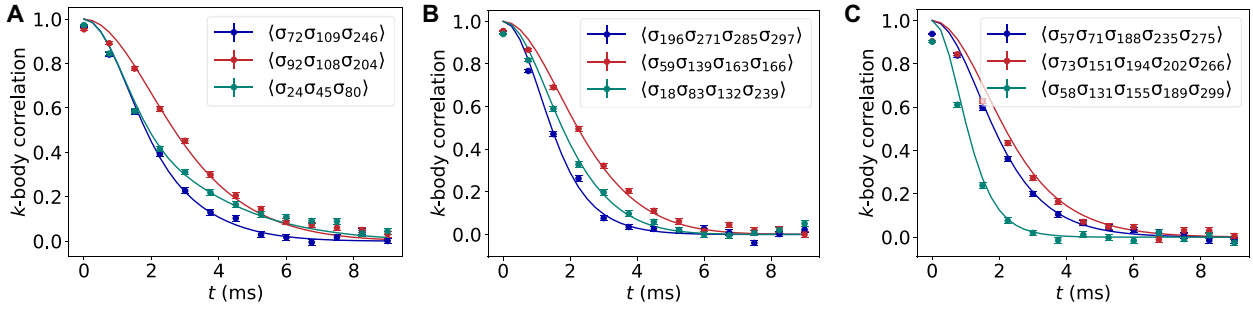

Fig. 4. Validation of the Hamiltonian learning results by higher-order correlations. We further use the Hamiltonian, learned from single-spin and two-spin observables, to predict *k*-body spin correlations with (**A**) $k = 3$, (**B**) $k = 4$, and (**C**) $k = 5$. We compare the theoretical predictions (solid curves) with experimental results (dots) for three randomly chosen sets of ion indices. Each experimental point is averaged over $M = 5640$ samples. Here, we use the Hamiltonian when the laser couples dominantly to the fifth highest phonon mode as an example.

$k = 3$, 4, and 5. For the arbitrarily chosen ion indices, we see good agreement between the theoretical and experimental results, which again shows the validity and the insignificant overfitting in the learning results.

DISCUSSION

To sum up, in this work we demonstrate the Hamiltonian learning of a long-range Ising model with $N = 300$ spins on a 2D ion trap quantum simulator. By exploiting global quantum operations and single-qubit–resolved measurements, we can learn a general Ising model with $O(N^2)$ parameters and the required sample size scales at most linearly with the qubit number. By independently calibrating the phonon modes of the ion crystal, a more efficient scheme with $O(N)$ parameters can achieve a similar value of the test error, although the fitting parameters may lack a good physical interpretation and may be related to the miscalibration of the phonon modes. In the future, by including higher-order nonlinear potential and the micromotion into the description of the phonon modes, we may improve the accuracy of the $O(1)$-scheme to be comparable to the $O(N^2)$-scheme and thus further enhance the efficiency of the Hamiltonian learning task.

Our method can also be extended to contain a site-dependent longitudinal field $H' = \sum_i h_i \sigma_z^i$, which is required in general applications like the formulation of a quadratic unconstrained binary optimization problem (*42*). Note that such a longitudinal field is canceled by the spin echo in our experimental sequence. Therefore, a straightforward method is to first use the sequence with the spin echo to learn all the Ising coupling coefficients J_{ij}'s and then fix them and execute another set of sequences without the spin echo to learn the additional N parameters h_i's, following the general analytical formulae in Materials and Methods.

The result of our Hamiltonian learning algorithm can directly be applied in quantum simulation (*10*–*13*) and quantum random sampling (*9*) tasks that are challenging for classical computers. As demonstrated in (*4*), the quasi-adiabatic evolution under a long-range transverse-field Ising model can be difficult to calculate classically when the system possesses, e.g., the competition between Ising interactions generated by different laser frequencies and/or long-range anti-ferromagnetic coupling due to a negative laser detuning. Note that, although qualitative information like the structure of the phonon modes may be obtained without knowing J_{ij}'s (*4*), detailed calibration of these parameters is a prerequisite for quantitative applications like finding approximate ground-state energies and spin configurations of the targeted classical Ising model. With future upgrades to support individually addressed single-qubit phase gates, the learning results can also enable the instantaneous quantum polynomial-time (IQP) circuit sampling, a well-known quantum random sampling scheme to demonstrate quantum advantage (*9*). Specifically, an instance of the IQP circuit $C = H^{\otimes N} D H^{\otimes N}$ can be achieved by a diagonal circuit D as the time evolution under the target Ising Hamiltonian in the σ_z basis together with random single-qubit phase gates and two layers of Hadamard gates by global microwave pulses. Similar to other quantum random sampling tasks (*5*–*9*), the verification of the sampling results requires accurate calibration of J_{ij}'s to allow the calculation of the cross-entropy benchmarks.

MATERIALS AND METHODS

Experimental setup

We use a monolithic 3D Paul trap (*4*, *43*, *44*) with a radio frequency (rf) of $\omega_{rf} = 2\pi \times 35.280$ MHz at a cryogenic temperature of 6.1 K. To obtain a 2D crystal of $N = 300$ $^{171}Yb^+$ ions, we use trap frequencies of $(\omega_x, \omega_y, \omega_z) = 2\pi \times (0.623, 2.20, 0.147)$ MHz where the z direction is the axial direction without micromotion as shown in Fig. 1A.

All the laser beams propagate in the micromotion-free directions in the yz plane to be insensitive to the inevitable micromotion of the 2D crystal along the x direction. We use a global 370-nm laser beam for Doppler cooling, optical pumping, and qubit state detection by turning on or off 14.7- and 2.1-GHz electro-optic modulators. Another two 370-nm laser beams are used for EIT cooling with π and σ^+ polarizations perpendicular to each other (*45*). They have a blue detuning of about 86 MHz from the transition between $|S_{1/2}, F = 1, m_F = 0\rangle$ ($|S_{1/2}, F = 1, m_F = -1\rangle$) and $|P_{1/2}, F = 0, m_F = 0\rangle$. We further use a global 411-nm laser beam with a linewidth of about 1 kHz, perpendicular to the ion crystal, for the sideband cooling of the transverse phonon modes.

The imaging system, with a numerical aperture of 0.33, is also perpendicular to the 2D ion crystal. We use a complementary metal-oxide semiconductor (CMOS) camera to collect the fluorescence from individual ions. We use electron shelving for the single-shot state detection by first converting the population in the $|S_{1/2}, F = 0, m_F = 0\rangle$ state to the $D_{5/2}$ and $F_{7/2}$ levels through global

411- and 3432-nm laser (*40*, *41*). Then, we count the fluorescence photon from individual ions under the global 370-nm laser with an exposure time of 1.5 ms. The SPAM infidelity is about 0.7%, mainly due to the imperfect shelving under inhomogeneous laser beams.

We use two counter-propagating 411-nm laser beams to generate the long-range Ising interaction. As shown in fig. S1, each laser beam has two frequency components on the two sides of the $|S_{1/2}, F=0, m_F=0\rangle$ to $|D_{5/2}, F=2, m_F=0\rangle$ transition, such that their time-independent ac Stark shift can be roughly canceled. On the other hand, the beat note of these two beams creates an ac Stark shift varying in time and space, which can create a spin-dependent force (*46*, *47*) and, further, an Ising-type spin-spin interaction when the phonon modes are adiabatically eliminated (*12*). More details about the daily operation of the 2D ion crystal and the derivation for the Ising model Hamiltonian can be found in our previous work (*4*).

Alignment of 2D ion crystal with laser wavefront

Equation 1 gives the theoretical Ising coupling coefficients when the laser phase is uniform over the 2D crystal. In practice, there can be misalignment between the 2D crystal and the equiphase surface of the laser, e.g., due to the tilting or twisting of the crystal. Then, each ion may have a site-dependent initial phase φ_i, and the theoretical Ising coupling will be modified into $J_{ij} \to J_{ij}\cos\left(\varphi_i - \varphi_j\right)$. Before the experiment, we adjust the laser wavefront and the 2D ion crystal to minimize such a site-dependent initial phase.

We calibrate the site-dependent φ_i by initializing all the ions in $|S_{1/2}, F=0, m_F=0\rangle$, applying a $\pi/2$ pulse using one 411-nm laser, and then applying another $\pi/2$ pulse using the other 411-nm laser with a random phase. The whole process can be understood as follows. Without loss of generality, we can use the first laser pulse to define the σ_x direction of the optical qubits between $|g\rangle \equiv |S_{1/2}, F=0, m_F=0\rangle$ and $|e\rangle \equiv |D_{5/2}, F=2, m_F=0\rangle$. Therefore, the first $\pi/2$ pulse prepares all the ions into $\left(|g\rangle + |e\rangle\right)/\sqrt{2}$. Then, the second laser pulse will have a phase shift of φ_i in the frame of individual ions, together with a global random phase of $\Delta\phi$, which we add purposely. This leads us to the final state $\left\{\left[1+e^{i(\varphi_i+\Delta\phi)}\right]|g\rangle + \left[1-e^{-i(\varphi_i+\Delta\phi)}\right]|e\rangle\right\}/2$.

From the above final product state, we can compute the expectation values

$$\langle \sigma_z^i \rangle = \cos\left(\varphi_i + \Delta\phi\right) \tag{2}$$

and

$$\begin{aligned}\langle \sigma_z^i \sigma_z^j \rangle &= \cos\left(\varphi_i + \Delta\phi\right)\cos\left(\varphi_j + \Delta\phi\right) \\ &= \frac{1}{2}\left[\cos\left(\varphi_i - \varphi_j\right) + \cos\left(\varphi_i + \varphi_j + 2\Delta\phi\right)\right]\end{aligned} \tag{3}$$

If we further average over the random phase $\Delta\phi$, then we have

$$\langle \sigma_z^i \sigma_z^j \rangle - \langle \sigma_z^i \rangle \langle \sigma_z^j \rangle = \frac{1}{2}\cos\left(\varphi_i - \varphi_j\right) \tag{4}$$

which can indicate whether the laser phase is uniform over the 2D crystal.

Once the above correlation matrix is measured for the $N = 300$ ions, we have two ways to minimize the misalignment: One is to rotate the ion crystal by electric fields, and the other is to rotate the laser beams. Because we want to keep the ion crystal to be micromotion-free along the transverse y direction, which already defines a plane at $y = 0$, here, we prefer to rotate the laser beams to suppress the spatial oscillation of the spin-spin correlation as much as possible. For the remaining phase fluctuation due to, e.g., the curvature of the laser wavefront, we use the voltages on the $4 \times 7 = 28$ dc segments together with an overall dc bias on the rf electrodes to fine-tune the shape of the 2D crystal. Typical measurement results for the final correlation matrix of $N = 300$ ions are shown in fig. S2, which indicates a nearly uniform optical phase over the 2D crystal.

Detection of change in the crystal configuration

As described in (*4*), the configuration of the 2D ion crystal of $N = 300$ ions has a typical lifetime of a few minutes under the Doppler cooling laser. However, during the experimental sequence, we need to turn off the cooling laser for the desired Hamiltonian evolution. Then, the ion configuration has a non-negligible probability to change during the evolution time up to 9 ms. In this experiment, although the global laser and the pattern of the few highest phonon modes are not sensitive to the small change in the ion positions, it does influence the site-resolved state detection of individual qubits. Therefore, we add a step to check the crystal configuration during the repetition of the experimental sequences. Specifically, we collect the fluorescence from individual ions during the Doppler cooling stage for each experimental trial using the CMOS camera. Ideally, all the ions will locate at the precalibrated positions and appear bright on the images. However, if the crystal configuration is changed, then some of these preselected regions will become empty and be detected as a dark ion.

Note that, under our experimental conditions, the probability for the configuration to change in each trial is still low. Therefore, once the configuration is changed, it will persist for several rounds of experimental sequences. This allows us to distinguish the configuration change from the occasional SPAM error on random ions. The detailed empirical criteria to identify the configuration change are shown in table S1. In addition, note that these criteria can discard not only the change in the ion configuration but also the occasional leakage to some metastable levels or the formation of, e.g., YbH^+ ions. In the experiment, we typically discard about 20% of the data, which depends on the conditions of the experimental setup.

Analytical formulae for *k*-body spin correlations

We consider a general Ising model Hamiltonian with a longitudinal field

$$H = H_0 + H' = \sum_{i<j} J_{ij}\sigma_z^i\sigma_z^i + \sum_i h_i\sigma_z^i \tag{5}$$

Following our experimental sequence, we initialize all the spins in $|+\rangle$, evolve the system under the Hamiltonian H for time t, and, lastly, measure the individual spins in the σ_x basis.

First, we consider the single-spin observables $\langle \sigma_x^i \rangle$. We have

$$\begin{aligned}\langle \sigma_x^i(t) \rangle &= \langle + \cdots + | e^{iHt}\sigma_x^i e^{-iHt} | + \cdots + \rangle \\ &= \frac{1}{2^n}\sum_{\{s\},\{s'\}} \langle \{s\} | e^{iHt}\sigma_x^i e^{-iHt} | \{s'\} \rangle \\ &= \frac{1}{2^n}\sum_{\{s\},\{s'\}} \langle \{s\} | e^{iE(\{s\})t}\sigma_x^i e^{-iE(\{s\prime\})t} | \{s'\} \rangle \\ &= \frac{1}{2^n}\sum_{\{s\}-s_i,s_i} \langle \{s\}-s_i | \langle s_i | e^{iE\left(\{s\}-s_i,s_i\right)t}\sigma_x^i e^{-iE\left(\{s\}-s_i,-s_i\right)t} | \{s\}-s_i \rangle | -s_i \rangle\end{aligned} \tag{6}$$

where $\{s\}$ represents the set of all spins in the σ_z basis, $\{s\} - s_i$ means the set of all but the ith spin, and we use the fact that σ_x^i flips the ith spin without affecting other spins.

In the above derivation, we use the function E to represent the energy of a given spin configuration. In general, if we divide the spins into two groups, $\{s_A\}$ and $\{s_B\}$, then we can express the total energy as

$$\begin{aligned} E(\{s\}) &= E_J(\{s\}) + E_h(\{s\}) \\ &= E_J(\{s_A\}) + E_J(\{s_B\}) + E_J(\{s_A\},\{s_B\}) + E_h(\{s_A\}) + E_h(\{s_B\}) \end{aligned} \tag{7}$$

where E_J and E_h represent the energy under the Ising interaction and the longitudinal field, respectively, and $E_J(\{s_A\},\{s_B\})$ is the interaction between the two groups. In addition, we have the symmetry

$$\begin{aligned} E_J(\{s\}) &= E_J(-\{s\}) \\ E_h(\{s\}) &= -E_h(-\{s\}) \\ E_J(\{s_A\},\{s_B\}) &= -E_J(\{s_A\},-\{s_B\}) = -E_J(-\{s_A\},\{s_B\}) \end{aligned} \tag{8}$$

Using these relations, we get

$$\begin{aligned} \langle \sigma_x^i(t)\rangle &= \frac{1}{2^n}\sum_{\{s\}-s_i,s_i} e^{iE(\{s\}-s_i,s_i)t} e^{-iE(\{s\}-s_i,-s_i)t} \\ &= \frac{1}{2^n}\sum_{\{s\}-s_i,s_i} e^{2i\left[E_J(\{s\}-s_i,s_i)+E_h(s_i)\right]t} \\ &= \frac{1}{2^n}\sum_{\{s\}} e^{2i\left(\sum_{k\neq i}J_{ki}s_k s_i + h_i s_i\right)t} \\ &= \frac{1}{2}\sum_{s_i} e^{2ih_i s_i t}\prod_{k\neq i}\cos\left(2J_{ki}s_i t\right) \\ &= \cos\left(2h_i t\right)\prod_{k\neq i}\cos\left(2J_{ki}t\right) \end{aligned} \tag{9}$$

Similarly, for the correlation between two spins i and j, we have

$$\begin{aligned} \langle \sigma_x^i(t)\sigma_x^j(t)\rangle &= \frac{1}{2^n}\sum_{\{s\}-s_i-s_j,s_i,s_j} e^{iE(\{s\}-s_i-s_j,s_i,s_j)t} e^{-iE(\{s\}-s_i-s_j,-s_i,-s_j)t} \\ &= \frac{1}{2^n}\sum_{\{s\}-s_i-s_j,s_i,s_j} e^{2i\left[E_J(\{s\}-s_i-s_j,s_i)+E_J(\{s\}-s_i-s_j,s_j)+E_h(s_i)+E_h(s_j)\right]t} \\ &= \frac{1}{2^n}\sum_{\{s\}} e^{2i\left(\sum_{k\neq i,j}J_{ki}s_k s_i + \sum_{k\neq i,j}J_{kj}s_k s_j + h_i s_i + h_j s_j\right)t} \\ &= \frac{1}{4}\sum_{s_i,s_j} e^{2i\left(h_i s_i + h_j s_j\right)t}\prod_{k\neq i,j}\cos\left[2\left(J_{ki}s_i + J_{kj}s_j\right)t\right] \\ &= \frac{1}{2}\cos\left[2\left(h_i+h_j\right)t\right]\prod_{k\neq i,j}\cos\left[2\left(J_{ki}+J_{kj}\right)t\right] \\ &\quad + \frac{1}{2}\cos\left[2\left(h_i-h_j\right)t\right]\prod_{k\neq i,j}\cos\left[2\left(J_{ki}-J_{kj}\right)t\right] \end{aligned} \tag{10}$$

In principle, by fitting the N single-spin magnetizations and the $N(N-1)/2$ two-spin correlations, we can get all the required parameters. In particular, if we focus on the early-time dynamics, then we have

$$\langle \sigma_x^i(t)\rangle \approx 1 - 2\left(h_i^2 + \sum_{k\neq i} J_{ki}^2\right)t^2 \tag{11}$$

and

$$\langle \sigma_x^i(t)\sigma_x^j(t)\rangle \approx 1 - 2\left[h_i^2 + h_j^2 + \sum_{k\neq i,j}\left(J_{ki}^2 + J_{kj}^2\right)\right]t^2 \tag{12}$$

Therefore, we have

$$\langle \sigma_x^i(t)\sigma_x^j(t)\rangle - \langle \sigma_x^i(t)\rangle\langle \sigma_x^j(t)\rangle \approx 4J_{ij}^2 t^2 \tag{13}$$

which already gives the magnitude of each desired J_{ij}. However, in practice, such early-time dynamics will be sensitive to the SPAM error, so we use the long-time evolution and the analytical formulae to fit the Ising coupling coefficients as described in the Experimental scheme section.

We can also generalize the above formulae to k-body correlations

$$\begin{aligned} \langle \sigma_x^{i_1}(t)\cdots\sigma_x^{i_k}(t)\rangle &= \frac{1}{2^n}\sum_{\{s\}} e^{2i\left(\sum_l{}' \sum_k J_{li_k}s_l s_{i_k} + \sum_k h_{i_k}s_{i_k}\right)t} \\ &= \frac{1}{2^k}\sum_{s_{i_1},\cdots,s_{i_k}} e^{2i\left(\sum_k h_{i_k}s_{i_k}\right)t}\prod_l{}'\cos\left[2\left(\sum_k J_{li_k}s_{i_k}\right)t\right] \\ &= \frac{1}{2^k}\sum_{s_{i_1},\cdots,s_{i_k}}\cos\left[2\left(\sum_k h_{i_k}s_{i_k}\right)t\right]\prod_l{}'\cos\left[2\left(\sum_k J_{li_k}s_{i_k}\right)t\right] \end{aligned} \tag{14}$$

where $'$ in the summation or production represents the set $\{s\} - s_{i_1} - \cdots - s_{i_k}$. The number of terms scales exponentially with k, so we do not use all of them for the Hamiltonian learning process but only use a few randomly chosen sets with $k = 3, 4,$ and 5 for the validation of our learning results.

In the above derivations, we assume ideal evolution under the Hamiltonian of Eq. 5, and we attribute the decay in the magnetization and the correlation to the dynamics under h_i's and J_{ij}'s. In practice, however, various noise sources can lead to decoherence in the experiment. For example, slow drifts in the laser intensity or frequency can lead to shot-to-shot fluctuation in these coefficients, which further translates into a Gaussian decay in the measured magnetizations and correlations. In addition, as we show in (*4*), the off-resonant phonon excitation can also be regarded as a spin dephasing term when we trace out the phonon modes. The actual error model can be very complicated depending on the contribution of different sources and will generally vary with different sites. Here, we take a simplified model with $2N$ parameters.

Specifically, for each ion i, we assign two parameters γ_{cor}^i and γ_{indep}^i for the correlated and independent decoherence rates, respectively. The correlated decoherence is motivated by the slow drift in the longitudinal fields caused by the global laser intensity. Although they average into a Gaussian decay over different experimental trials through $\langle \cos(ht)\rangle = e^{-(\gamma t)^2/2}$ when $h \sim N(0,\gamma^2)$, still, the coherence between different ions is maintained when we consider spin-spin correlations. In contrast, the independent decoherence captures the other error sources that do not maintain the phase coherence among ions. With such terms included and with the longitudinal field set to

zero, the theoretical dynamics for single-spin and multi-spin observables become

$$\langle\sigma_x^i(t)\rangle=\exp\left\{-\left[\left(\gamma_{\text{indep}}^i\right)^2+\left(\gamma_{\text{cor}}^i\right)^2\right]t^2\right\}\cdot\prod_{k\neq i}\cos\left(2J_{ki}t\right) \quad (15)$$

$$\begin{aligned}\langle\sigma_x^i(t)\sigma_x^j(t)\rangle=&\frac{1}{2}\exp\left\{-\left[\left(\gamma_{\text{indep}}^i\right)^2+\left(\gamma_{\text{indep}}^j\right)^2+\left(\gamma_{\text{cor}}^i+\gamma_{\text{cor}}^j\right)^2\right]t^2\right\}\\&\times\prod_{k\neq i,j}\cos\left[2\left(J_{ki}+J_{kj}\right)t\right]\\&+\frac{1}{2}\exp\left\{-\left[\left(\gamma_{\text{indep}}^i\right)^2+\left(\gamma_{\text{indep}}^j\right)^2+\left(\gamma_{\text{cor}}^i-\gamma_{\text{cor}}^j\right)^2\right]t^2\right\}\\&\times\prod_{k\neq i,j}\cos\left[2\left(J_{ki}-J_{kj}\right)t\right]\end{aligned} \quad (16)$$

$$\begin{aligned}\langle\sigma_x^{i_1}(t)\cdots\sigma_x^{i_k}(t)\rangle=&\frac{1}{2^k}\sum_{s_{i_1},\cdots,s_{i_k}}\exp\\&\left\{-\left[\sum_k\left(\gamma_{\text{indep}}^{i_k}\right)^2+\left(\sum_k\gamma_{\text{cor}}^{i_k}s_{i_k}\right)^2\right]t^2\right\}\\&\times\prod_l{}'\cos\left[2\left(\sum_k J_{li_k}s_{i_k}\right)t\right]\end{aligned} \quad (17)$$

If we fit these $2N$ parameters together with the Ising coupling coefficients, because their leading-order effects are both the decay in the magnetization and correlation as shown by Eqs. 11 and 12, then it will largely increase the uncertainty in the learning results. Instead, here, we first fit all the γ_{cor}^i's and γ_{indep}^i's with fixed $J_{ij}=0$ by setting a large laser detuning of 80 kHz above the COM mode. Then, we fix these fitted decoherence rates during the rest of the experiment to learn the desired Hamiltonian when the laser detuning is closer to some of the phonon modes. Note that this separated calibration step is consistent with our error model of a slow drift in the laser-induced ac Stark shift (the longitudinal field) and an additional independent dephasing due to noise sources other than the laser. The calibration results for γ_{cor}^i's and γ_{indep}^i's are shown in fig. S3. Together, they give an average decoherence time of about $1/\sqrt{\left(\gamma_{\text{indep}}^i\right)^2+\left(\gamma_{\text{cor}}^i\right)^2}\sim 9$ ms.

Compensating the leakage error to $D_{5/2}$ and $F_{7/2}$ levels

Under the off-resonant 411-nm laser, there is a small probability that the final population will be in the $D_{5/2}$ or $F_{7/2}$ levels, which is a leakage error from the qubit subspace in the $S_{1/2}$ levels. In the experiment, we observe a gradual increase in the leakage probability with the evolution time, which mainly comes from the spontaneous emission from the $D_{5/2}$ levels to the $F_{7/2}$ levels. After electron shelving, such leaked population will be detected as dark, that is, the $|0\rangle\equiv|S_{1/2},F=0,m_F=0\rangle$ state. This will cause bias in the measured magnetizations and correlations.

For small leakage probability ϵ_{L}, we can measure the leakage rate experimentally and correct it to the first order during the experimental sequence. The idea is to divide the experimental trials into two groups. For one group, we use the original experimental sequence in Fig. 1B. For the other group, we insert a π pulse to exchange the $|0\rangle\equiv|S_{1/2},F=0,m_F=0\rangle$ and $|1\rangle\equiv S|_{1/2},F=1,m_F=0\rangle$ states before the measurement. Suppose, ideally, the ith qubit has probability p_0^i to be in $|0\rangle$ and probability p_1^i to be in $|1\rangle$ ($p_0^i+p_1^i=1$), and suppose, now, there is probability ϵ_{L}^i of the leakage error that may vary for different ions. Now, if we evaluate $\langle\sigma_z^i\rangle$ for the two groups of datasets, then we will get $\left(p_0^i-p_1^i\right)\left(1-\epsilon_{\text{L}}^i\right)+\epsilon_{\text{L}}^i$ and $\left(p_1^i-p_0^i\right)\left(1-\epsilon_{\text{L}}^i\right)+\epsilon_{\text{L}}^i$, respectively, without or with the π pulse. From their average, we obtain the leakage probability ϵ_{L}^i, while their difference gives $2\left(p_0^i-p_1^i\right)\left(1-\epsilon_{\text{L}}^i\right)$, which is proportional to the ideal single-spin magnetization $p_0^i-p_1^i$ and can be recovered by dividing $\left(1-\epsilon_{\text{L}}^i\right)$. Following similar derivations, we can use this method to correct the k-body spin correlations $\langle\sigma_z^{i_1}(t)\cdots\sigma_z^{i_k}(t)\rangle$ to the first order by dividing $\prod_{l=1}^k\left(1-\epsilon_{\text{L}}^{i_l}\right)$.

For each ion, we can further perform a linear fit for the leakage probability versus time and obtain the leakage rates shown in fig. S4. The central ions feel higher 411-nm laser intensity and typically have higher leakage rates, with a typical timescale above 30 ms, much longer than our evolution time.

Theoretical scaling of the precision

As described in the Experimental scheme section, we use the relative energy difference $\epsilon\left[J^{(1)},J^{(2)}\right]\equiv\langle|E\left[J^{(1)}\right]-E\left[J^{(2)}\right]|\rangle/\sqrt{\delta E\left[J^{(1)}\right]\cdot\delta E\left[J^{(2)}\right]}$ between the learning results $J_{ij}^{(1)}$'s and $J_{ij}^{(2)}$'s on independent datasets to characterize the learning precision. Specifically, for any given spin configuration $\{s\}$, we can evaluate the energy for the two Hamiltonians $E\left[\{s\};J^{(1)}\right]$ and $E\left[\{s\};J^{(2)}\right]$. Then, we compute the numerator as the average of $|E\left[\{s\};J^{(1)}\right]-E\left[\{s\};J^{(2)}\right]|$ over the randomly sampled spin configurations, and we define $\delta E\left[J^{(1)}\right]$ and $\delta E\left[J^{(2)}\right]$ as the SDs of $E\left[\{s\};J^{(1)}\right]$ and $E\left[\{s\};J^{(2)}\right]$ over random spin configurations.

Next, we analyze the scaling of the precision ϵ versus the system size N. When fitting the $O\left(N^2\right)$ parameters of J_{ij}'s, the different parameters are correlated through their covariance matrix, so we expect their fluctuation to be on the same order which we denote as $\delta J_{ij}\sim\delta$. We have $\delta\propto 1/\sqrt{M}$ depending on the sample size M. Now, if we compute the energy difference due to the δJ_{ij} terms on random spin configurations, then we are basically performing a random walk with $O\left(N^2\right)$ steps. Therefore, the numerator can be estimated to be $O(N\delta)$. On the other hand, for the denominator, we consider two cases: (i) We couple dominantly to a single-phonon mode such that we have an all-to-all coupling $J_{ij}\sim O\left(J_0\right)$, and (ii) we couple to all the phonon modes with roughly a power-law decay $J_{ij}\sim J_0/\|\vec{r}_i-\vec{r}_j\|^\alpha$ (*12*). In both cases, to observe nontrivial dynamics in the magnetizations and correlations, we want $\sum_{k\neq i}J_{ik}^2T^2\sim O(1)$ according to Eqs. 11 and 12 where T is the total evolution time. In the first case, it means $J_0\sim 1/\sqrt{N}T$, and, in the second case, it gives $J_0\sim 1/T$. In both cases, after averaging over random spin configurations, we find the SD of the total energy to be $O\left(\sqrt{N}/T\right)$; thus, the precision will scale as $\sqrt{N}\delta T$.

On the other hand, if the ground-state properties are desired, then, in the denominator, we should not compare with the fluctuation of the energy but with the ground-state energy itself. Suppose there to be no notable frustration, we expect the ground-state energy to scale at least as $O(N)$, then the precision will be $O(1)$, no longer degrading with the system size.

Fitting anharmonic trap potential

To compute the Ising coupling coefficients theoretically using Eq. 1, we need to know the accurate phonon mode structure of the ion crystal, which is, in principle, a classical problem and can be solved given the external trap potential. The trap potential is, in principle, governed by the design of the trap electrodes and the voltages that we apply on them. However, because of the fabrication errors and various experimental noises, the theoretically computed trap potential can often deviate from the actual one. Therefore, we choose to fit the trap potential from the available information, including the measured ion positions in the 2D crystal at the precision of about 1 μm, the frequencies of a few resolvable phonon modes at the precision of about 1 kHz and the excitation pattern of these modes. As the phonon spectrum becomes denser at the low-frequency side, here, we only use the frequencies of the 10 highest modes and one lowest frequency. In addition, we can apply a weak global 411-nm laser pulse on the blue sideband of a resolved mode k, and then the excitation probability of each ion i will be proportional to b_{ik}^2.

Often, a harmonic trap is still a reasonable approximation to the trap potential, and, here, we add a few anharmonic terms as small perturbation. In particular, we assume that the potential can be described by some low-order polynomials that vary slowly in space. Otherwise, if the potential is fast oscillating from ion to ion, then there will be too many parameters to fit from the available information.

Even if we truncate to quartic polynomials, the potential already contains a large number of parameters and a straightforward fitting will be both inefficient and likely to be trapped to unphysical local minima. Instead, we divide the fitting procedure into five stages as shown in table S2.

In the first stage, we give an initial fitting of the harmonic terms x^2 and z^2 within the plane of the 2D ion crystal. The y^2 term is measured as the single-ion trap frequency along the perpendicular y axis through the resolved sideband transition with high precision and is fixed during the whole fitting procedure. For any given coefficients for the x^2 and z^2 terms, we use the measured ion positions as the starting point to search the equilibrium positions under their Coulomb interaction and further solve the collective phonon mode frequencies. Then, we compare them with the measured values and further improve the fitting results by minimizing this cost function.

In the second stage, we add cubic terms to better fit the ion positions inside the xz plane. Because the equilibrium positions of all the ions have $y = 0$, we can drop all the terms containing y and only consider x^3, x^2z, xz^2, and z^3 terms.

However, the cubic terms are not sufficient to give a good fitting to the ion positions and mode frequencies, so we further consider the quartic terms. To have a good starting point to fit the quartic terms as perturbations, we insert the third stage to refine the quadratic terms with the previous cubic terms fixed. Then, in the fourth stage, we add some quartic terms. Because of the reflection symmetry of the designed electrodes, here, we only consider symmetric terms like y^2z^2, y^2x^2, x^2z^2, and z^4, and we expect the other asymmetric terms to be subdominant. The asymmetry of the ion crystal can already be captured by the cubic terms above. In addition, here, we drop the x^4 term because the size the 2D crystal is much smaller in the x direction than that in the z direction.

In the last stage, we further fit cubic terms along the y direction through their influence to the transverse phonon modes. Here, we focus on xy^2 and zy^2 terms, which can be regarded as a site-dependent trap frequency along the y direction. They will not change the equilibrium positions of the ions but will affect the phonon modes. On the other hand, terms like x^2y, z^2y, and xyz correspond to a site-dependent force perpendicular to the crystal. Their main effect is a twist in the crystal that cannot be measured from the image of the ions. In addition, after the small twist of the crystal, these forces are already canceled by the harmonic terms as well as the Coulomb interaction between ions, so we expect their influence on the phonon modes to be higher order and, hence, do not include them in this fitting. Last, the y^3 does not affect the equilibrium positions or the transverse phonon modes and, therefore, is not considered either.

In the above fitting, we do not consider the micromotion of the ions because, in our case, the largest micromotion amplitude is still smaller than the inter-ion distance. In the future, we may also take the micromotion into consideration to get a more accurate description of the phonon modes for larger ion crystals (*48*–*50*).

Supplementary Materials

This PDF file includes:

Tables S1 and S2
Figs. S1 to S4

REFERENCES AND NOTES

1. Y. Kim, A. Eddins, S. Anand, K. X. Wei, E. van den Berg, S. Rosenblatt, H. Nayfeh, Y. Wu, M. Zaletel, K. Temme, A. Kandala, Evidence for the utility of quantum computing before fault tolerance. *Nature* **618**, 500–505 (2023).
2. D. Bluvstein, S. J. Evered, A. A. Geim, S. H. Li, H. Zhou, T. Manovitz, S. Ebadi, M. Cain, M. Kalinowski, D. Hangleiter, J. P. Bonilla Ataides, N. Maskara, I. Cong, X. Gao, P. Sales Rodriguez, T. Karolyshyn, G. Semeghini, M. J. Gullans, M. Greiner, V. Vuletić, M. D. Lukin, Logical quantum processor based on reconfigurable atom arrays. *Nature* **626**, 58–65 (2024).
3. J. G. Bohnet, B. C. Sawyer, J. W. Britton, M. L. Wall, A. M. Rey, M. Foss-Feig, J. J. Bollinger, Quantum spin dynamics and entanglement generation with hundreds of trapped ions. *Science* **352**, 1297–1301 (2016).
4. S.-A. Guo, Y.-K. Wu, J. Ye, L. Zhang, W.-Q. Lian, R. Yao, Y. Wang, R.-Y. Yan, Y.-J. Yi, Y.-L. Xu, B.-W. Li, Y.-H. Hou, Y.-Z. Xu, W.-X. Guo, C. Zhang, B.-X. Qi, Z.-C. Zhou, L. He, L.-M. Duan, A site-resolved two-dimensional quantum simulator with hundreds of trapped ions. *Nature* **630**, 613–618 (2024).
5. F. Arute, K. Arya, R. Babbush, D. Bacon, J. C. Bardin, R. Barends, R. Biswas, S. Boixo, F. G. S. L. Brandao, D. A. Buell, B. Burkett, Y. Chen, Z. Chen, B. Chiaro, R. Collins, W. Courtney, A. Dunsworth, E. Farhi, B. Foxen, A. Fowler, C. Gidney, M. Giustina, R. Graff, K. Guerin, S. Habegger, M. P. Harrigan, M. J. Hartmann, A. Ho, M. Hoffmann, T. Huang, T. S. Humble, S. V. Isakov, E. Jeffrey, Z. Jiang, D. Kafri, K. Kechedzhi, J. Kelly, P. V. Klimov, S. Knysh, A. Korotkov, F. Kostritsa, D. Landhuis, M. Lindmark, E. Lucero, D. Lyakh, S. Mandrà, J. R. McClean, M. McEwen, A. Megrant, X. Mi, K. Michielsen, M. Mohseni, J. Mutus, O. Naaman, M. Neeley, C. Neill, M. Y. Niu, E. Ostby, A. Petukhov, J. C. Platt, C. Quintana, E. G. Rieffel, P. Roushan, N. C. Rubin, D. Sank, K. J. Satzinger, V. Smelyanskiy, K. J. Sung, M. D. Trevithick, A. Vainsencher, B. Villalonga, T. White, Z. J. Yao, P. Yeh, A. Zalcman, H. Neven, J. M. Martinis, Quantum supremacy using a programmable superconducting processor. *Nature* **574**, 505–510 (2019).
6. H.-S. Zhong, H. Wang, Y.-H. Deng, M.-C. Chen, L.-C. Peng, Y.-H. Luo, J. Qin, D. Wu, X. Ding, Y. Hu, P. Hu, X.-Y. Yang, W.-J. Zhang, H. Li, Y. Li, X. Jiang, L. Gan, G. Yang, L. You, Z. Wang, L. Li, N.-L. Liu, C.-Y. Lu, J.-W. Pan, Quantum computational advantage using photons. *Science* **370**, 1460–1463 (2020).
7. Y. Wu, W.-S. Bao, S. Cao, F. Chen, M.-C. Chen, X. Chen, T.-H. Chung, H. Deng, Y. Du, D. Fan, M. Gong, C. Guo, C. Guo, S. Guo, L. Han, L. Hong, H.-L. Huang, Y.-H. Huo, L. Li, N. Li, S. Li, Y. Li, F. Liang, C. Lin, J. Lin, H. Qian, D. Qiao, H. Rong, H. Su, L. Sun, L. Wang, S. Wang, D. Wu, Y. Xu, K. Yan, W. Yang, Y. Yang, Y. Ye, J. Yin, C. Ying, J. Yu, C. Zha, C. Zhang, H. Zhang, K. Zhang, Y. Zhang, H. Zhao, Y. Zhao, L. Zhou, Q. Zhu, C.-Y. Lu, C.-Z. Peng, X. Zhu, J.-W. Pan, Strong quantum computational advantage using a superconducting quantum processor. *Phys. Rev. Lett.* **127**, 180501 (2021).
8. L. S. Madsen, F. Laudenbach, M. F. Askarani, F. Rortais, T. Vincent, J. F. F. Bulmer, F. M. Miatto, L. Neuhaus, L. G. Helt, M. J. Collins, A. E. Lita, T. Gerrits, S. W. Nam, V. D. Vaidya, M. Menotti, I. Dhand, Z. Vernon, N. Quesada, J. Lavoie, Quantum computational advantage with a programmable photonic processor. *Nature* **606**, 75–81 (2022).

9. D. Hangleiter, J. Eisert, Computational advantage of quantum random sampling. *Rev. Mod. Phys.* **95**, 035001 (2023).
10. J. I. Cirac, P. Zoller, Goals and opportunities in quantum simulation. *Nat. Phys.* **8**, 264–266 (2012).
11. I. M. Georgescu, S. Ashhab, F. Nori, Quantum simulation. *Rev. Mod. Phys.* **86**, 153–185 (2014).
12. C. Monroe, W. C. Campbell, L.-M. Duan, Z.-X. Gong, A. V. Gorshkov, P. W. Hess, R. Islam, K. Kim, N. M. Linke, G. Pagano, P. Richerme, C. Senko, N. Y. Yao, Programmable quantum simulations of spin systems with trapped ions. *Rev. Mod. Phys.* **93**, 025001 (2021).
13. K. Bharti, A. Cervera-Lierta, T. H. Kyaw, T. Haug, S. Alperin-Lea, A. Anand, M. Degroote, H. Heimonen, J. S. Kottmann, T. Menke, W.-K. Mok, S. Sim, L.-C. Kwek, A. Aspuru-Guzik, Noisy intermediate-scale quantum algorithms. *Rev. Mod. Phys.* **94**, 015004 (2022).
14. M. Nielsen, I. Chuang, *Quantum Computation and Quantum Information* (Cambridge Univ. Press, ed. 10, 2000).
15. M. P. da Silva, O. Landon-Cardinal, D. Poulin, Practical characterization of quantum devices without tomography. *Phys. Rev. Lett.* **107**, 210404 (2011).
16. N. Wiebe, C. Granade, C. Ferrie, D. G. Cory, Hamiltonian learning and certification using quantum resources. *Phys. Rev. Lett.* **112**, 190501 (2014).
17. M. Holzäpfel, T. Baumgratz, M. Cramer, M. B. Plenio, Scalable reconstruction of unitary processes and hamiltonians. *Phys. Rev. A* **91**, 042129 (2015).
18. S.-T. Wang, D.-L. Deng, L.-M. Duan, Hamiltonian tomography for quantum many-body systems with arbitrary couplings. *New J. Phys.* **17**, 093017 (2015).
19. J. Wang, S. Paesani, R. Santagati, S. Knauer, A. A. Gentile, N. Wiebe, M. Petruzzella, J. L. O'Brien, J. G. Rarity, A. Laing, M. G. Thompson, Experimental quantum hamiltonian learning. *Nat. Phys.* **13**, 551–555 (2017).
20. S. Krastanov, S. Zhou, S. T. Flammia, L. Jiang, Stochastic estimation of dynamical variables. *Quantum Sci. Technol.* **4**, 035003 (2019).
21. P.-Y. Hou, L. He, F. Wang, X.-Z. Huang, W.-G. Zhang, X.-L. Ouyang, X. Wang, W.-Q. Lian, X.-Y. Chang, L.-M. Duan, Experimental hamiltonian learning of an 11-qubit solid-state quantum spin register. *Chin. Phys. Lett.* **36**, 100303 (2019).
22. X.-L. Qi, D. Ranard, Determining a local Hamiltonian from a single eigenstate. *Quantum* **3**, 159 (2019).
23. E. Bairey, I. Arad, N. H. Lindner, Learning a local hamiltonian from local measurements. *Phys. Rev. Lett.* **122**, 020504 (2019).
24. T. J. Evans, R. Harper, S. T. Flammia, Scalable bayesian hamiltonian learning. arXiv:1912.07636 [quant-ph] (2019).
25. E. Bairey, C. Guo, D. Poletti, N. H. Lindner, I. Arad, Learning the dynamics of open quantum systems from their steady states. *New J. Phys.* **22**, 032001 (2020).
26. A. A. Gentile, B. Flynn, S. Knauer, N. Wiebe, S. Paesani, C. E. Granade, J. G. Rarity, R. Santagati, A. Laing, Learning models of quantum systems from experiments. *Nat. Phys.* **17**, 837–843 (2021).
27. A. Valenti, G. Jin, J. Léonard, S. D. Huber, E. Greplova, Scalable hamiltonian learning for large-scale out-of-equilibrium quantum dynamics. *Phys. Rev. A* **105**, 023302 (2022).
28. T. E. O'Brien, L. B. Ioffe, Y. Su, D. Fushman, H. Neven, R. Babbush, V. Smelyanskiy, Quantum computation of molecular structure using data from challenging-to-classically-simulate nuclear magnetic resonance experiments. *PRX Quantum* **3**, 030345 (2022).
29. W. Yu, J. Sun, Z. Han, X. Yuan, Robust and efficient Hamiltonian learning. *Quantum* **7**, 1045 (2023).
30. M. K. Joshi, C. Kokail, R. van Bijnen, F. Kranzl, T. V. Zache, R. Blatt, C. F. Roos, P. Zoller, Exploring large-scale entanglement in quantum simulation. *Nature* **624**, 539–544 (2023).
31. J. Haah, R. Kothari, E. Tang, Learning quantum hamiltonians from high-temperature gibbs states and real-time evolutions. *Nat. Phys.* **20**, 1027–1031 (2024).
32. A. Bakshi, A. Liu, A. Moitra, E. Tang, Structure learning of hamiltonians from real-time evolution. arXiv:2405.00082 (2024).
33. M. Saffman, Quantum computing with atomic qubits and rydberg interactions: Progress and challenges. *J. Phys. B: At. Mol. Opt. Phys.* **49**, 202001 (2016).
34. X. Wu, X. Liang, Y. Tian, F. Yang, C. Chen, Y.-C. Liu, M. K. Tey, L. You, A concise review of rydberg atom based quantum computation and quantum simulation. *Chin. Phys. B* **30**, 020305 (2021).
35. S. Ebadi, T. T. Wang, H. Levine, A. Keesling, G. Semeghini, A. Omran, D. Bluvstein, R. Samajdar, H. Pichler, W. W. Ho, S. Choi, S. Sachdev, M. Greiner, V. Vuletić, M. D. Lukin, Quantum phases of matter on a 256-atom programmable quantum simulator. *Nature* **595**, 227–232 (2021).
36. C. Senko, J. Smith, P. Richerme, A. Lee, W. C. Campbell, C. Monroe, Coherent imaging spectroscopy of a quantum many-body spin system. *Science* **345**, 430–433 (2014).
37. B.-W. Li, Y.-K. Wu, Q.-X. Mei, R. Yao, W.-Q. Lian, M.-L. Cai, Y. Wang, B.-X. Qi, L. Yao, L. He, Z.-C. Zhou, L.-M. Duan, Probing critical behavior of long-range transverse-field ising model through quantum kibble-zurek mechanism. *PRX Quantum* **4**, 010302 (2023).
38. C. H. Baldwin, B. J. Bjork, M. Foss-Feig, J. P. Gaebler, D. Hayes, M. G. Kokish, C. Langer, J. A. Sedlacek, D. Stack, G. Vittorini, High-fidelity light-shift gate for clock-state qubits. *Phys. Rev. A* **103**, 012603 (2021).
39. C. Roman, A. Ransford, M. Ip, W. C. Campbell, Coherent control for qubit state readout. *New J. Phys.* **22**, 073038 (2020).
40. C. L. Edmunds, T. R. Tan, A. R. Milne, A. Singh, M. J. Biercuk, C. Hempel, Scalable hyperfine qubit state detection via electron shelving in the $^2D_{5/2}$ and $^2F_{7/2}$ manifolds in $^{171}yb^+$. *Phys. Rev. A* **104**, 012606 (2021).
41. H.-X. Yang, J.-Y. Ma, Y.-K. Wu, Y. Wang, M.-M. Cao, W.-X. Guo, Y.-Y. Huang, L. Feng, Z.-C. Zhou, L.-M. Duan, Realizing coherently convertible dual-type qubits with the same ion species. *Nat. Phys.* **18**, 1058–1061 (2022).
42. A. Lucas, Ising formulations of many np problems. *Front. Phys.* **2**, 10.3389/fphy.2014.00005 (2014).
43. M. Brownnutt, G. Wilpers, P. Gill, R. C. Thompson, A. G. Sinclair, Monolithic microfabricated ion trap chip design for scaleable quantum processors. *New J. Phys.* **8**, 232 (2006).
44. Y. Wang, M. Qiao, Z. Cai, K. Zhang, N. Jin, P. Wang, W. Chen, C. Luan, B. Du, H. Wang, Y. Song, D. Yum, K. Kim, Coherently manipulated 2d ion crystal in a monolithic paul trap. *Adv. Quantum Technol.* **3**, 2000068 (2020).
45. L. Feng, W. L. Tan, A. De, A. Menon, A. Chu, G. Pagano, C. Monroe, Efficient ground-state cooling of large trapped-ion chains with an electromagnetically-induced-transparency tripod scheme. *Phys. Rev. Lett.* **125**, 053001 (2020).
46. D. Leibfried, B. DeMarco, V. Meyer, D. Lucas, M. Barrett, J. Britton, W. M. Itano, B. Jelenković, C. Langer, T. Rosenband, D. J. Wineland, Experimental demonstration of a robust, high-fidelity geometric two ion-qubit phase gate. *Nature* **422**, 412–415 (2003).
47. P. J. Lee, K.-A. Brickman, L. Deslauriers, P. C. Haljan, L.-M. Duan, C. Monroe, Phase control of trapped ion quantum gates. *J. Opt. B Quantum Semiclass. Opt.* **7**, S371–S383 (2005).
48. Y.-K. Wu, Z.-D. Liu, W.-D. Zhao, L.-M. Duan, High-fidelity entangling gates in a three-dimensional ion crystal under micromotion. *Phys. Rev. A* **103**, 022419 (2021).
49. H. Landa, M. Drewsen, B. Reznik, A. Retzker, Modes of oscillation in radiofrequency Paul traps. *New J. Phys.* **14**, 093023 (2012).
50. H. Landa, M. Drewsen, B. Reznik, A. Retzker, Classical and quantum modes of coupled Mathieu equations. *J. Phys. A Math. Theor.* **45**, 455305 (2012).

Acknowledgments

Funding: This work was supported by Innovation Program for Quantum Science and Technology (2021ZD0301601 and 2021ZD0301605), the Ministry of Science and Technology of China (2021AAA0150000), the Shanghai Qi Zhi Institute, Tsinghua University Initiative Scientific Research Program, and the Ministry of Education of China. L.-M.D. acknowledges in addition support from the New Cornerstone Science Foundation through the New Cornerstone Investigator Program. Y.-K.W. acknowledges in addition support from Tsinghua University Dushi program. C.Z. acknowledges support from the Shui-Mu Scholar postdoctoral fellowship from Tsinghua University. P.-Y.H. acknowledges the start-up fund from Tsinghua University. **Author contributions:** L.-M.D. proposed and supervised the project. S.-A.G., J.Y., L.Z., Y.W., W.-Q.L., R.Y., Y.-L.X., C.Z., Y.-Z.X., B.-X.Q., P.-Y.H., L.H., and Z.-C.Z. carried out the experiment. Y.-K.W. developed the associated theory. S.-A.G., J.Y., and Y.-K.W. analyzed the data. Y.-K.W., S.-A.G., and L.-M.D. wrote the manuscript. **Competing interests:** Y.W., W.-Q.L., R.Y., and C.Z. are affiliated with HYQ Co. Y.-K.W., Y.W., W.-Q.L., R.Y., Y.-Z.X., B.-X.Q., L.H., Z.-C.Z. and L.-M.D. hold shares with HYQ Co. The other authors declare that they have no competing interests. **Data and materials availability:** All data needed to evaluate the conclusions in the paper are present in the paper and/or the Supplementary Materials.

Submitted 27 September 2024
Accepted 30 December 2024
Published 29 January 2025
10.1126/sciadv.adt4713